Formation and ordering of topological defect arrays produced by dilatational strain and shear flow in smectic-*A* liquid crystals

Sourav Chatterjee
Department of Mechanical Engineering, Carnegie Mellon University, Pittsburgh, Pennsylvania 15213, USA

Shelley L. Anna*
Department of Mechanical Engineering and Department of Chemical Engineering, Carnegie Mellon University, Pittsburgh, Pennsylvania 15213, USA

(Received 27 April 2011; revised manuscript received 23 July 2011; published 9 January 2012)

A microscale shear cell is used to study the formation of parabolic focal conic defects in the thermotropic smectic-*A* liquid crystal 8CB (4-octyl-4′-cyanobiphenyl). Defects are produced by four distinct methods: by the application of dilatational strain alone, by shear flow alone, by dilatational strain and subsequent shear flow, and by the simultaneous application of dilatational strain and shear flow. We confirm that defects originate within the bulk, consistent with the previously suggested undulation instability mechanism. In the presence of a shear flow, we observe that defect formation requires micrometer-level dilatations, whose magnitude depends on the sample thickness. The size and ordering of both disordered and ordered defect arrays is quantified using a pair distribution function. Deviations from the predictions of linear stability theory are observed that have not been reported previously. For example, defects form a square array with greater ordering in the principal flow direction. Ordering due to shear flow does not change the average defect size. It has been shown previously that the principal defect sizes of ordered defects scale differently with sample thickness than the wavelength of the small amplitude undulations. We find that disordered defects show a similar deviation from this predicted wavelength.

DOI: 10.1103/PhysRevE.85.011701 PACS number(s): 61.30.Jf, 47.57.Lj, 61.30.Pq, 83.80.Xz

I. INTRODUCTION

A number of macromolecular systems [1] form the lamellar or smectic phase, with their molecules arranged in parallel layers. Parallel lamella are unstable, and upon application of external stress, the layers undergo sinusoidal undulations [2,3] to relieve the external stress. These undulations, known as the undulation instability, are characteristic of lamellar microstructures [4] and can be observed in thermotropic smectic liquid crystals [2], lyotropics [5,6], cholesterics [7], block copolymers [8], aqueous DNA solutions [9], and columnar liquid crystals [10]. The growth of the instability, in thermotropics, leads to micrometer-scale defect textures known as parabolic focal conic defects [11]. Parabolic focal conic defects can be produced by various methods of deforming the sample [11–13], and the textures can form highly ordered patterns [12]. Ordered defect textures produced in this way have been used as templates for soft lithography [14,15]. However, the size and ordering of these defect textures has not been quantified as a function of the deformation methods used to produce them. Most reported studies of size and ordering focus on linear stability analyses near the stability threshold [2,11,16].

The present paper reports an experimental study of defect textures produced in the thermotropic smectic-*A* liquid crystal 8CB (4-octyl-4′-cyanobiphenyl) in a microscale shear cell. In the smectic-*A* phase of 8CB, the rodlike molecules within each smectic layer are aligned perpendicular to the layer. The sample is confined between rigid parallel plates with sample thicknesses of hundreds of micrometers, and defects are generated using four different methods of deformation: (i) by the application of dilatational strain to the sample, (ii) by the application of shear flow, (iii) by the application of dilatational strain and subsequent shear flow, and (iv) by the simultaneous application of dilatational strain and shear flow. We characterize the defect textures for each method of deformation using the pair distribution function to quantify the size and the ordering of the defect textures, and comparing the results with predictions from linear stability theory.

The undulation instability arises in smectic phases because layer dilatation requires much more energy than layer curvature [17]. Hence, when a smectic-*A* sample is confined between two parallel plates with its layers oriented parallel to the plate, the layers respond to dilatational strain by forming periodic undulations. The undulations vary in amplitude across the sample thickness with the largest amplitude at the center of the cell, and vanishing amplitude at the plate surfaces. Linear stability analysis predicts that the undulation instability takes place at a critical dilatation δ_c of the order of the interlayer separation (typically a few angstroms), and this has been confirmed by light scattering [2,18,19].

The focal conic defects that develop in these lamellar materials are of the order of tens of micrometers in size, and they are often assumed to arise from the undulation instability. A number of studies [5,6,20,21] have argued that the spherulite-shaped "onion" textures observed during the shear flow of lyotropic liquid crystals [20] form due to the undulation instability. In thermotropic smectic-*A* liquid crystals, lipid-based liquid crystals [22], and dilute solutions of lyotropics [23], the undulations give rise to parabolic focal conic defects. In thermotropic liquid crystals, parabolic focal conic defects can also be produced as a result of shear flow [13]. In the presence of a shear flow without dilatational strain,

*Author to whom correspondence should be addressed: sanna@cmu.edu

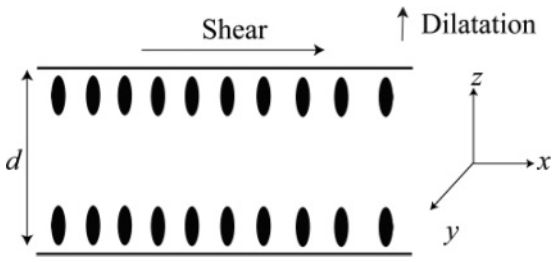

FIG. 1. Schematic diagram of shear flow and anchoring conditions. The principal flow direction is along the x axis and the neutral direction is along the y axis. Dilatation occurs along the z axis and the xy plane of the sample is visualized.

the defects appear to stream from surface irregularities. This may be a result of dilatation of the layers near the surface irregularity inducing localized undulations. Thus, while it has been conjectured that parabolic focal conic defects originate from undulations [11,24], the mechanism of defect formation appears to be different in the case of defects formed due to dilatational strain compared with those formed in the presence of a shear flow.

Although the most unstable wavelength near the stability threshold is well described by linear stability analysis [25–27], the change in layer structure during the growth of the instability is not well understood [28]. Linear stability analysis of the undulation instability induced by the simultaneous application of dilatational strain and shear flow [16] predicts the formation of perfectly square arrays of parabolic focal conic defects with sizes equivalent to those formed in the absence of shear flow. Experimentally observed sizes of ordered defects deviate from this prediction [12]. It is not clear whether this difference in size is due to the applied shear flow, or a change in scaling during the nonlinear growth of the instability. Similarly, visual observations suggest a square ordering [12], but the ordering has not been quantified.

In the present paper, we investigate the formation of defect textures using a custom-built shear cell, shown schematically in Fig. 1. The smectic sample is confined between two parallel plates separated by a gap of the order of hundreds of micrometers. A linear Couette flow is applied in the x direction with a constant strain rate, and a dilatational strain is applied in the z direction. Homeotropic anchoring is imposed at the surfaces of both plates. The defect dynamics are visualized in real time using a high-speed camera.

A similar shear cell with visualization capabilities and homeotropic surface anchoring was used previously to produce ordered textures of smectic liquid crystals [12,29]. The authors used plate separations of 70 μm $< d <$ 420 μm, a similar range to that considered here. Horn and Kleman [13,30] used a modified cone and plate rheometer with homeotropic boundary conditions at the two surfaces to study the formation of defects by shear flow alone. The plate separation in a cone and plate geometry varies with radial distance from the axis, rendering it difficult to examine the dependence on sample thickness. Larson and Mather [31] conducted visualization studies of disordered smectic defect textures confined between two parallel disks. Shear cells have also been used to study defect dynamics in cholesteric liquid crystals [32] and nematic liquid crystalline polymers [33].

The defects are identified by the characteristic pattern produced by parabolic focal conic defects (PFCD) when viewed between crossed polarizers. The PFCD texture shown in Fig. 2(a) has been observed in thermotropics [11,12], lyotropics [23,34–36], liquid crystalline polymers [37], and cellulose nanocrystals [38]. A parabolic focal conic defect consists of smectic layers wrapped around two singularity lines. The singularity lines form two parabolas oriented in perpendicular planes that each pass through the focal point of the other, as Fig. 2(b) illustrates schematically. The defects are arranged in a dense lattice. When defects are formed by pure dilatational strain, the lattice forms a polygonal texture, described in detail by Rosenblatt *et al.* [11] Simultaneous application of dilatational strain and shear flow leads to a square lattice texture [12], with its principal directions aligned with the flow and neutral directions [16]. The square lattice is illustrated schematically in Fig. 2(c) and is formed by the intersections of the crossed parabolas at the midplane of the sample. Figure 2(a) shows a polarization microscopy image of the square grid, with the top and bottom of each parabola marked for the purpose of illustration. The structure of the three-dimensional grid has been described elsewhere [11,22,38,39].

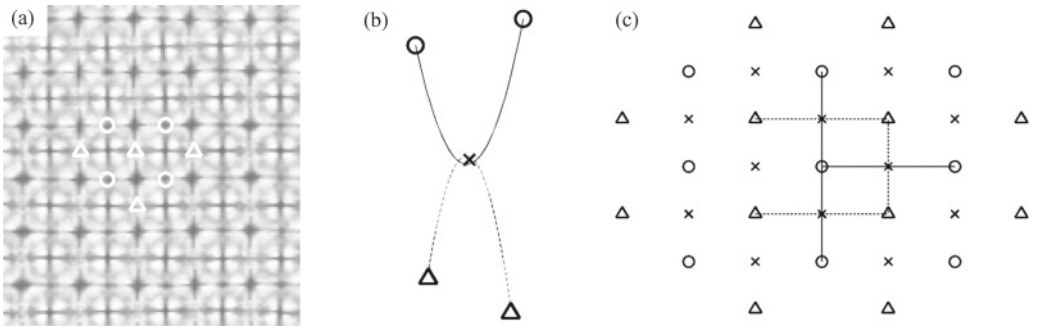

FIG. 2. (a) An image of a parabolic focal conic defect array as viewed from the top using polarized light microscopy, with the ends of the upward-facing parabolas (○) and the downward facing parabolas (Δ) marked. (b) Each defect in this lattice consists of two parabolic singularity lines oriented at right angles to each other with each parabola passing through the focal point of the other. (c) Two-dimensional view from the top depicting the arrangement of parabolic focal conic defects in a square array. Circles (○) denote the ends of the upward facing parabolas. Triangles (Δ) denote the ends of the downward facing parabolas. Crosses (×) denote the locations of the intersections of the parabolas.

The present paper describes our experimental observations of the formation of defect textures, and quantification of their size and ordering, as a function of the deformation method used to generate the textures. Section II provides details describing the materials and methods used to conduct and analyze the experiments. Section III describes and discusses the results of the measurements and analysis, and Sec. IV offers concluding remarks.

II. METHODS AND MATERIALS

In the present study, we examine defect formation in the smectic-A phase of the small molecule thermotropic liquid crystal 8CB (4-octyl-4′-cyanobiphenyl). 8CB exists in the smectic-A phase at room temperature, and undergoes a transition to the nematic phase at 33.5 °C and a transition to the isotropic phase at 40.5 °C. At 25 °C, the penetration length of 8CB is $\lambda = 7$ Å [24].

We use a custom-built shear cell to investigate the dynamics of texture formation. The shear cell is built on the translation stage of an inverted microscope, allowing the layer structure to be visualized in real time during the application of a shear flow or dilatational strain. The sample is confined between two parallel plates that are separated by a distance d that varies as $100\ \mu\text{m} < d < 500\ \mu\text{m}$. The lower plate is held fixed while the upper plate is moved laterally using a stepper motor-controlled linear stage (Newmark Systems NLS4 stage). The motor can control the motion in steps of 13 μm. The described configuration leads to a simple Couette flow profile between the parallel plates. In this flow, the strain is given by

$$\gamma = \frac{L}{d}, \tag{1}$$

and the strain rate is given by

$$\dot{\gamma} = \frac{U}{d}, \tag{2}$$

where L is the time-dependent distance traveled by the upper plate, U is the constant velocity of the upper plate, and d is the sample thickness. Experiments are performed in the strain rate range $0.1 < \dot{\gamma} < 5\ \text{s}^{-1}$ for total strains of $0.5 < \gamma < 5$ strain units. The top plate moves in the x direction, which is the principle flow direction. The y direction is the neutral direction and the z direction is the velocity gradient direction. A dilatational strain is applied in the z direction using a micrometer. The dilatational strain is applied by moving the micrometer dial manually in increments of 1 μm. We use the term "dilatation", δ, in this study to refer to the distance in micrometers moved by the upper plate in the $+z$ direction. The associated dilatational strain ε is given by

$$\varepsilon = \frac{\delta}{d}. \tag{3}$$

The assembled shear cell is affixed to the translation stage of the microscope and a region of the sample is viewed by transmitted light. The layer structure can be visualized in real time, during the application of a shear flow or dilatational strain.

As Fig. 1 indicates, homeotropic boundary conditions are imposed at both plate surfaces, so that the rodlike liquid crystal molecules are oriented perpendicular to the plates. The glass plates are prepared by sonication in soapy water and rinsing with isopropyl alcohol and acetone. Homeotropic anchoring is imposed by the adsorption of a surface active layer. Following a procedure similar to Ignes-Mullol *et al.* [40], the cleaned glass plates are dipped in a 0.002 wt% cetyltrimethylammonium bromide (CTAB) solution (Sigma Aldrich), and withdrawn slowly. Before the start of each experiment, the anchoring is verified by placing the sample between crossed polarizers when the sample is in the smectic phase and observing complete extinction, indicating parallel layers with molecules aligned perpendicular to the plates.

The sample is heated by applying a voltage across the indium tin oxide (ITO) plate that is used as the top plate. Prior to the start of the experiment, the sample is heated well into the isotropic phase (42 °C) and cooled back to room temperature (25 °C), where the sample has transitioned to the smectic phase. The rates of heating and cooling are approximately 2 °C/min.

The sample is viewed using an inverted microscope (Nikon Eclipse TE2000U) with a polarizer and analyzer inserted into the optical path on either side of the sample. Images are recorded using a high-speed camera (IDT X4, Redlake, Inc.). Images are captured at a magnification of 30×, where each pixel corresponds to 0.55 μm on each side. This magnification provides ample resolution to characterize the micrometer-sized defect textures.

We analyze the captured images in several ways to quantify the defect size and ordering. From a raw image such as that shown in Fig. 2(a), we construct a binary image with a white background and single black pixel located at the parabola intersection for each PFCD. We note that the upper parabolas are oriented along the flow (x) direction. The fast Fourier transform (FFT) of the images is obtained using built-in MATLAB subroutines, resulting in a centered plot of the logarithm of the magnitudes of the Fourier components.

The pair distribution function $g(\vec{r})$, also known as the pair correlation function, is defined as the probability of finding a defect location at position $\vec{r}$, given that there exists a defect location at the origin $\vec{r} = 0$ [41]. The distribution is normalized by its value for a perfectly random sample. In our case,

$$g(\vec{r}) = g(r,\theta). \tag{4}$$

To separately quantify both the radial and angular structure of $g(\vec{r})$, we calculate two special cases, namely the orientational distribution function $g(\theta)$ and the radial distribution function $g(r)$.

To calculate the orientational distribution function, we first designate one defect as the origin. The region around the defect is divided into area sectors with an arc of 5°.The number of defects in the area sector for the reference defect is counted. The procedure is repeated for each defect in the image, and the average number of defects in an area sector is computed for all defects in the image. Edge effects are taken into account by including in the normalization only those defects whose area sectors lie entirely within the image domain. The sum of the count is calculated for several values of the radial distance from each defect, and normalized by the total area dA_i of each area sector. Furthermore, since the image has a finite area, we have calculated the distributions for defect singularities in five different images, and then computed the average over the total

image area. Thus, we average over $p = 5$ images to obtain

$$g(\theta) = \frac{\sum_{i=1}^{p}\left[\sum_{r=r_{\min}}^{r_{\max}} g_i(r,\theta)\right]}{\rho \sum_{i=1}^{p} dA_i}, \tag{5}$$

where ρ is the number density defined as

$$\rho = \frac{\sum_{i=1}^{p} D_i}{\sum_{i=1}^{p} IA_i}. \tag{6}$$

D_i is the number of singularities in each image and IA_i is the total area of each image. Angular binning is selected such that $\theta = 0^\circ$, 90°, 180°, and 270° are located at the centers of their respective bins, allowing any order anisotropy in the flow direction to be interpreted with minimal effect of finite binning. The resolution of the angular grid is limited by the pixel resolution of the captured image. A finer angular grid with angular spacing less than 5° would result in wedge perimeters that are less than one pixel at the radial location of the measurement.

In order to calculate the radial distribution function $g(r)$, we count the defects that lie within a thin strip at a fixed radial distance from each defect center and then normalize by the area of the radial strip $2\pi r dr$. Edge effects are taken into account by including only those sectors whose area lies entirely within the image boundary. Finally, we average over multiple images by normalizing the results over the total number of singularities and the number density given in Eq. (6) where

$$g(r) = \frac{\sum_{i=1}^{p}\left[\sum_{\theta=0}^{2\pi} g_i(r,\theta)\right]}{p(2\pi r dr)\rho}. \tag{7}$$

III. RESULTS

In this section, we study the formation of defect textures using the microscale shear cell depicted in Fig. 1. Using four different methods to deform the smectic sample, we generate arrays of parabolic focal conic defects. Figure 3 shows polarization images of typical defect arrays formed using these methods. We use four different methods: (i) the application of dilatational strain alone, (ii) the application of shear flow alone, (iii) the application of dilatational strain and subsequent shear flow, and (iv) the simultaneous application of dilatational strain and shear flow. Each of these methods has been described previously [11–13]. We compare the resulting defect texture for each of these four cases.

When the sample experiences a shear flow alone, with no accompanying dilatational strain, we observe an array of PFCDs ordered in a nearly square pattern aligned in the flow direction, as shown in Fig. 3(a). A similar experiment was previously performed by Horn and Kleman [13] in a cone

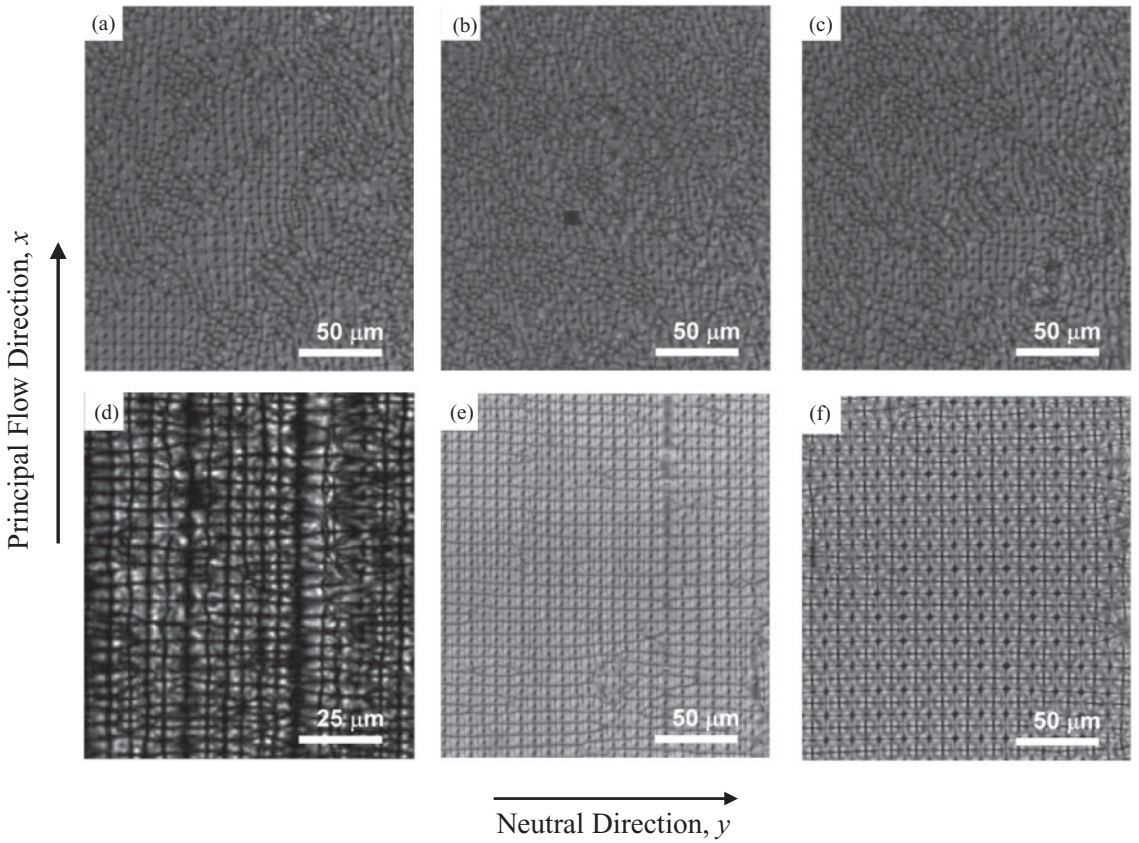

FIG. 3. Images depicting arrays of parabolic focal conic defects when defects are produced by (a) application of dilatational strain only. (b) and (c) correspond to textures obtained after 1.33 and 3.5 strain units on the texture shown by (a). (d) Defects produced by the application of shear flow only and no dilatational strain. (e) Defects produced by the simultaneous application of dilatational strain and shear flow for $d = 100$ μm. (f) Defects produced in the same manner as (e) for $d = 350$ μm.

and plate rheometer. Defects formed this way are not very reproducible, and do not form homogeneously throughout the sample. Instead, the defects are much more prevalent near the edges of the sample where surface irregularities are more common. This is consistent with the observations of Horn and Kleman [13] who observe the formation of defects triggered by dust particles in the sample.

When the sample is subject to dilatational strain alone, with no shear flow, we observe a disordered array of PFCDs as shown in Fig. 3(b), where the sample thickness is $d = 150\ \mu$m and the dilatation applied is $\delta = 7\mu$m, corresponding to a dilatational strain of $\varepsilon = 0.047$. This result is consistent with that of Rosenblatt *et al.* [11] who performed a similar experiment.

Once the disordered array is formed, it cannot be ordered by subsequent shearing. When a shear flow is applied, we observe qualitative changes in the structure, but the sample does not become well ordered. Figures 3(c) and 3(d) show a typical result for postdilatational shearing for the same sample as in Fig. 3(b) after 1.33 and 3.5 strain units, respectively. A similar observation was made by Oswald *et al.* [12], but the authors did not characterize the resulting structure quantitatively.

The most highly ordered defect textures are produced by the simultaneous application of dilatational strain and shear flow. The sample is dilated using a micrometer at the same time that a shear rate is applied using the linear stepper motor. The sample is dilated slowly in increments of 1 μm during the application of the shear flow. We observe that a quasistatic dilatation of the sample is needed to produce a highly ordered texture, since a fast dilatation of the sample does not allow for the relaxation of the defect texture via ordering.

Examples of two resulting defect arrays using sample thicknesses of 100 and 300 μm are shown in Figs. 3(e) and 3(f). The defects are highly monodisperse in size and form a nearly square array. This enhanced order was previously described by Oswald *et al.* [12] who performed a similar experiment to produce highly ordered defect arrays. The characteristic size of the individual defects in the array increases with sample thickness.

The visual observations described above are substantiated using the Fourier transforms of the images, shown in Fig. 4. Figure 4(a) shows the FFT of the image in Fig. 3(b), where defects are formed by a dilatational strain only. There are no visible peaks in the FFT, indicating the absence of order. Figure 4(b) shows the FFT of the image in Fig. 3(d). There are four peaks at right angles to one another, indicating square ordering. Beyond the first peak, there are no higher-order peaks, indicating partial alignment due to the shear flow. Finally, Fig. 4(c) shows the FFT of the image in Fig. 3(f), where defects are produced by simultaneous dilatational strain and shear flow. Multiple sharp peaks in the intensity pattern are observed, indicating a high degree of ordering. The primary peak in Fig. 4(c) is also much sharper than that in Fig. 4(b), further indicating a high degree of ordering obtained by simultaneous dilatational strain and shear flow.

The observations show that the simultaneous action of dilatational strain and shear flow leads to defect arrays that are highly ordered, reproducible, and have a tunable periodicity via the sample thickness. The application of shear flow after the formation of defects does not lead to well aligned samples, and the application of shear flow alone does not produce reproducible defect textures. These observations have been noted in the literature [11–13] but have not been quantified experimentally.

Rosenblatt *et al.* [11] suggested that the defect textures originate from the sinusoidal undulations of the smectic layers above a critical dilatation δ_c of the order of angstroms. This mechanism is supported by light scattering studies [19], suggesting that the defects originate within the bulk of the sample, and not at the surface, where the undulation amplitude vanishes due to the imposed homeotropic anchoring at the rigid flat surface. However, when PFCD structures are produced by shear flow alone, such as in the experiments of Horn and Kleman [13] and in our experiments shown in Fig. 3(a), the focal conic domains are observed to stream from surface irregularities. Horn and Kleman [13] demonstrate, through a series of images, the nucleation of focal conic domains around a dust particle.

For the case where defects are formed by dilatational strain only, similar to [11], where disordered, polygonal arrays of PFCDs are observed [Fig. 3(b)], we test whether defects form as a result of surface irregularities or bulk undulations by comparing the locations of the individual defects within the texture for two successive experiments for the same sample

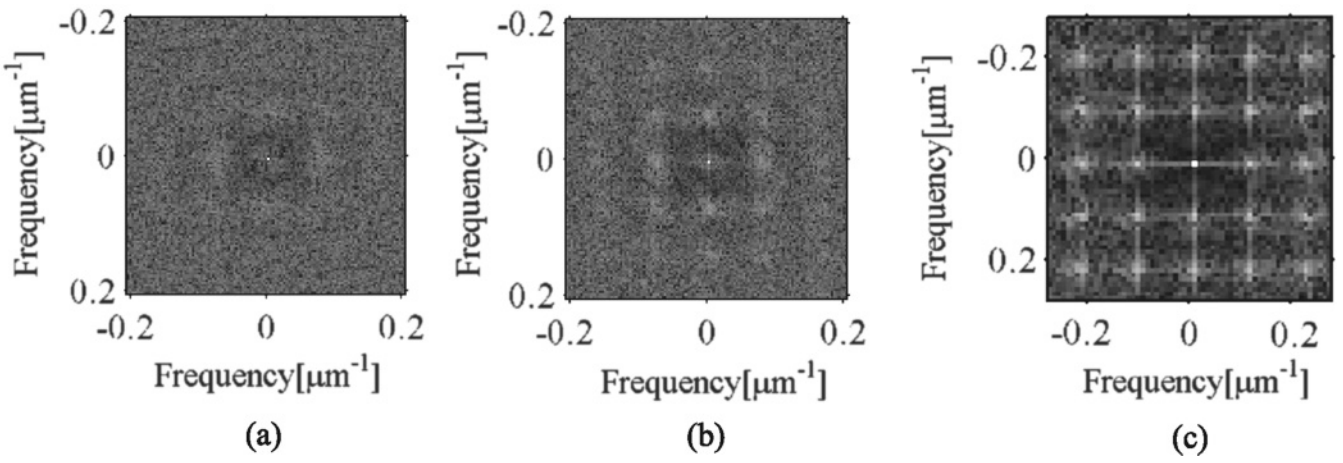

FIG. 4. Fast Fourier transforms of the defect textures produced by (a) Fig. 3(b), (b) Fig. 3(c), and (c) Fig. 3(f).

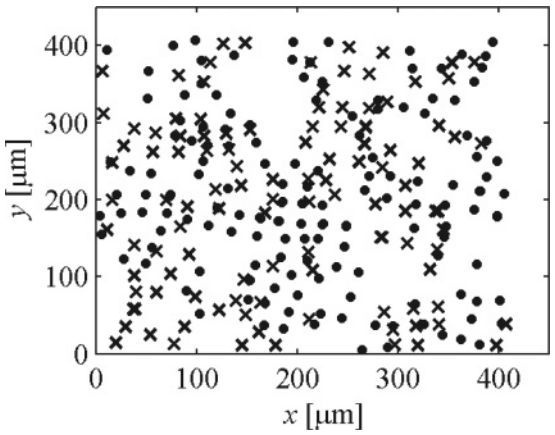

FIG. 5. Positions of defect centers for two successive dilatation experiments for the same sample loading. The sample was heated into the isotropic phase (≈42 °C at 2 °C/min) and subsequently cooled to the smectic phase (≈25 °C at −2 °C/min) in between the two experiments.

loading. The sample thickness is 300 μm and the amount of dilatation applied is $\delta = 4\mu$m ($\varepsilon = 0.0133$). In between the two experiments the sample is heated to the isotropic phase (42 °C) and cooled back to the smectic phase (25 °C) at heating and cooling rates of 2 °C/min. At 42 °C, we observe a clear liquid characteristic of the isotropic phase upon removal of the polarizer and analyzer from the optical path. With the polarizer and analyzer inserted and crossed, we observe complete extinction. This confirms that the smectic layering has completely melted in between the two experiments. However, the anchoring conditions and the surface irregularities remain the same for both experiments since the sample is not reloaded. In Fig. 5, we show the locations of the defects for the two successive experiments. The locations of the defect centers for the first experiment are indicated by the crosses and for the second experiment they are indicated by the filled circles. We observe that the defect positions for the successive experiments are not correlated, suggesting that defects originate within the bulk and not as a result of surface irregularities. These results are repeatable for experiments performed on multiple samples, with the same rates of heating and cooling. These experiments are consistent with the hypothesis of Rosenblatt *et al.* [11] that defects originate in the bulk and not from surface irregularities. We presume that the origination of the defects within the bulk when dilatational strain is applied is the reason why PFCD arrays are more uniform and reproducible throughout the sample compared with production by shear flow alone.

In the case when dilatational strain is applied alone, defects form easily, requiring only small levels of dilatation of less than 1 μm regardless of sample thickness. This is consistent with the undulation instability that occurs at angstrom-level dilatations, well below the resolution of our micrometer [11,19]. This condition is considerably modified when dilatational strain and shear flow are simultaneously applied, resulting in ordered PFCD arrays. We observe that the presence of the shear flow retards the formation of PFCDs such that the amount of dilatation required to form visible defect textures is of the order of a few micrometers, i.e., about three orders of magnitude larger than the critical strain needed to induce the undulation instability.

The amount of dilatation required to form defects is also a function of the sample thickness. We recorded the dilatational strain at which defects form as a function of sample thickness. The sample initially exhibits complete extinction when viewed between crossed polarizers. We apply Couette flow with a constant shear rate and extend the maximum strain applied using a triangular saw tooth strain profile where $V = 50\ \mu$m/s, the maximum strain for each cycle is 300 μm, and four cycles are applied. We dilate the sample by 1 μm between the second and third cycle. We repeat this shear flow–dilatation sequence, dilating the sample by 1 μm during each sequence. The procedure is repeated until we observe a change in the sample intensity (birefringence), indicating the formation of parabolic focal conic defects. The change in intensity is not gradual, but rather, the birefringence increases sharply at a critical dilatation. The dilatation at which the change in birefringence occurs is reproducible, and decreases with an increase in sample thickness. We refer to this sudden change in birefringence as the "formation of visible defects." This is consistent with previous reports of a saturation phase [12], where the defect intensity is observed to gradually increase with an increase in dilatation when the defects are formed by pure dilatational strain, and a sudden increase in intensity to the saturation phase is observed when defects are formed by simultaneous application of dilatational strain and shear flow. This is likely due to the annihilation of the unsaturated defects by the shear flow.

The critical dilatation for formation of visible defects is plotted as a function of sample thickness in Fig. 6. The error bars shown in the figure indicate the variation in the required critical dilatation for different sample loadings. Figure 6 shows that the required dilatation δ required to produce PFCD arrays decreases with sample thickness. For a 100-μm-thick sample, a PFCD pattern is not observed until nearly 10 μm of dilatation has been imposed, representing a nearly 10% dilatational strain. The amount of required dilatation δ decreases nearly linearly with increasing sample thickness up to a sample thickness of 300 μm. For sample thicknesses greater than 300 μm, less than 1 μm of dilatation is needed to form visible defect patterns, representing a dilatational strain of less than 0.33%. Since the smallest dilatation we can apply

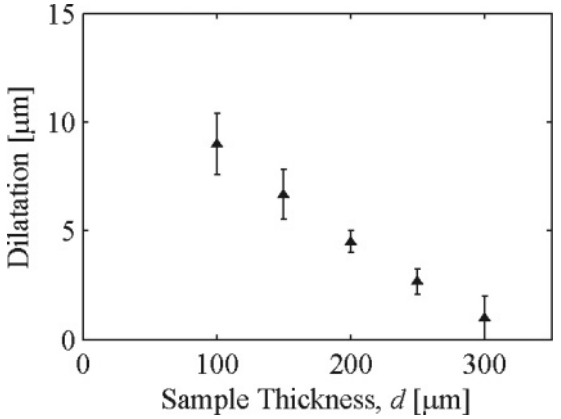

FIG. 6. Amount of dilatation required to form parabolic focal conic defects in the presence of a shear flow, as a function of the sample thickness.

using our instrumentation is 1 μm, we cannot make accurate measurements for sample thicknesses greater than 300 μm. Thus, for thicker samples, we say that defects form readily upon the application of a shear flow.

These observations can be understood qualitatively by considering the competing forces within the shear cell. PFCD formation is favored since it minimizes the total free energy of the layered liquid crystal sample. However, in thin samples, surface anchoring competes with layer deformation, introducing an energy penalty associated with the curvature of layers near the surface. As the sample thickness increases, surface anchoring becomes less important compared with curvature energies in the bulk. Hence PFCD formation will be more favorable and less dilatation will be required to form visible PFCD textures for thicker samples. This hypothesis also suggests that the surface anchoring energy may play an important role in determining the critical dilatation. Oswald *et al.* [12] formed ordered arrays of PFCDs in a very similar manner. However, they do not report values for the critical dilatation required to form defects. In that study, the authors imposed homeotropic anchoring by coating the plates with polysilane [12], which likely has a different anchoring energy than the CTAB solution used here. Although the anchoring energies are not known in the present experiments nor in those of Ref. [12], we hypothesize that a smaller anchoring energy would result in a smaller variation in the dilatation required to form visible defect patterns. This hypothesis remains to be tested. We note here that surface anchoring in smectics entails additional considerations compared with nematics due to the layered structure. For example, tilted anchoring in a smectic would require melting of the layers in the vicinity of the rigid plates in order to satisfy boundary conditions on the molecular orientation [42]. Surface-induced smectic ordering at surfaces imposing tilted anchoring is intimately connected with bulk tilt elastic constants that arise to maintain the layer normal orientation of smectic-*A* molecules [43]. We do not attempt to decouple the anchoring energy for a tilted surface and the bulk tilt elastic constant in this work; rather we note that the role of surface anchoring in the formation of toroidal focal conic defect textures is well documented [42,44] and hence its importance cannot be neglected in microscale gaps where the elastic and anchoring energies compete with each other [42].

To quantify the defect size and ordering, we use the pair correlation function $g(\vec{r})$. The pair correlation function is often used to describe atomic configurations [45] and size [46] and ordering [41] of colloidal particles; here we employ it in the analysis of focal conic defect textures. Figure 7(a) shows the angular component of the pair distribution function, $g(\theta)$, for a sample thickness of 200 μm. The pair distribution function has been obtained by analyzing multiple images with the same sample thickness. The sharp peaks at right angles to one another indicate square ordering. The smaller peaks also suggest square ordering, since their angles correspond to those obtained in a square lattice: 22.5°, 45°, and 67.5°. The pair distribution function shows that the defects are ordered in a square lattice with principal directions aligned with the flow and velocity gradient directions. This is consistent with the visual observations and the FFT patterns in Figs. 3(b), 3(c), and 4(f).

We further observe that the peaks in the direction of flow ($\theta = \pm 90°$) are greater in height than the peaks in the neutral direction ($\theta = 0°, 180°$). The difference in peak heights between the flow and the neutral directions are shown for different sample thicknesses in Fig. 7(b). The difference in peak heights is always positive, confirming that there is systematically greater order in the flow direction compared with the neutral direction. This anisotropy in the square pattern is in contrast to predictions of linear stability theory. For example, Oswald and Ben-Abraham [16] predict that defects will form a square lattice with two equivalent principal directions, corresponding to the flow and velocity gradient directions. While the linear stability analysis corresponds to conditions near the stability threshold, it appears that the nonlinear growth of the instability leads to a shear flow-induced anisotropy in the fully formed PFCD arrays.

Closer examination of the polarization images of the PFCD arrays reveals the source of the ordering anisotropy. Figure 8 shows a typical image of a square PFCD array formed by simultaneous application of shear flow and dilatational strain. Imperfections in the square array are apparent in the image, in which a row of PFCD defects comes to an end and the rows of defects on either side of the partial row come together to heal the defect. This structure is analogous to edge dislocations observed in arrays of atoms [47]. Figure 8

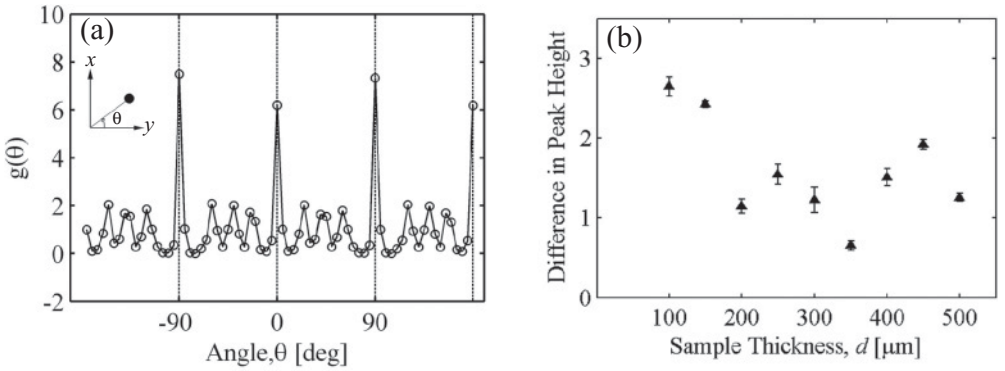

FIG. 7. The pair distribution function for defects formed by the simultaneous action of dilatational strain and shear flow for $d = 300$ μm. (a) Angular dependence of the pair distribution function for the defect centers. Inset defines the angle θ relative to the flow direction. $\theta = 0^o$ corresponds to the flow direction. $\theta = 90^o$ corresponds to the neutral direction, perpendicular to flow. (b) The difference in the maximum peak height between the velocity direction and the neutral direction as a function of sample thickness.

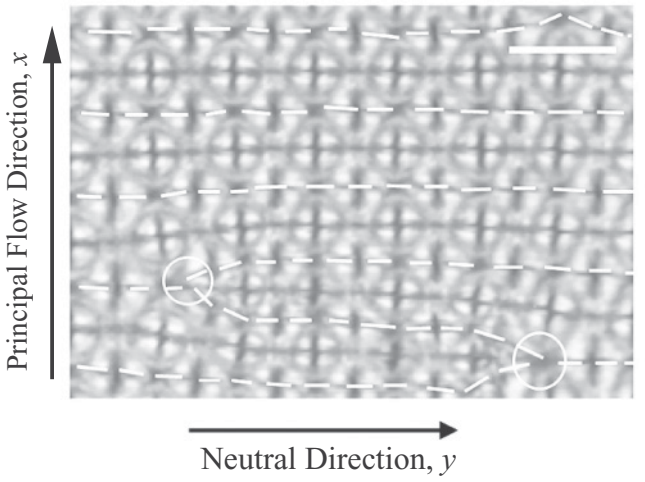

FIG. 8. Close-up image of an ordered array of parabolic focal conic defects produced in the same manner as Fig. 5(b) for $d = 200\ \mu$m. Dashed lines are drawn between rows of defects in the neutral direction. Dislocations can occur in the defect array where a row of defects ends, as indicated by the encircled regions. The scale bar is 25 μm.

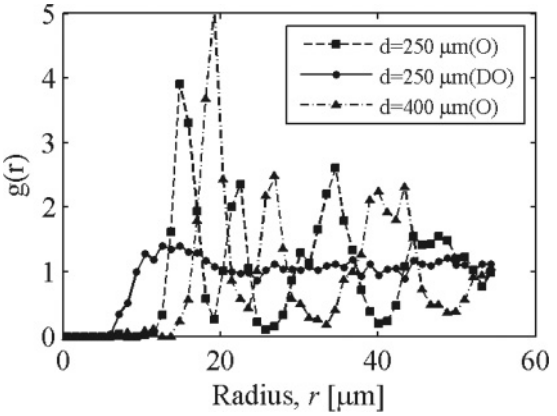

FIG. 9. Radial dependence of the pair distribution function. "O" refers to ordered defects formed by the simultaneous action of dilatational strain and shear flow, and "DO" refers to the disordered defects formed by dilatational strain only.

shows one such array-level "dislocation," where we use the term "dislocation" to specify imperfections in the focal conic defect array, not imperfections in the molecular ordering of the smectic. We have traced the rows of singularity lines using dashed white lines to guide the eye, and the dislocation has been encircled for the purposes of illustration. By identifying multiple dislocations over a larger sample area than that shown, we have confirmed that the orientation of the dislocation shown here is representative of the orientations observed throughout the sample. Dislocations can be described by a Burgers vector, which represents the magnitude and direction of the lattice distortion due to the dislocation. In this case, the Burgers vectors of the dislocations are directed systematically along the principal flow direction. The distortion of the lattice along the flow direction results in more bond vectors occurring along the principal flow direction than along the neutral direction, consistent with the greater peak heights in the principal flow direction shown in the angular distribution function of Fig. 7. A similar analysis was conducted for block copolymer films oriented in shear flows [48] where, in the case of a hexagonal lattice, a higher frequency of bond vectors was systematically observed in the direction perpendicular to flow and a preferential orientation of the Burgers vector of the dislocation was related to this result. Directional anisotropy of "dislocations" within PFCD arrays has not been reported previously.

Previous measurements of the sizes of ordered defects produced by simultaneous dilatational strain and shear flow [12] indicate that the increase in defect size with sample thickness follows an empirical relationship with a different functional form than that of the undulations analyzed by linear stability theory. The sizes of disordered defects formed by dilatational strain alone have not been measured as a function of sample thickness. Thus, it is not clear whether the deviation from the scaling of the undulation instability arises due to the later stages of the growth of the undulations or due to the presence of shear flow, which could alter the sizes of the defects. To quantify the dependence of the defect size distribution on sample thickness for ordered as well as disordered defect arrays, we examine the radial distribution function $g(r)$, shown in Fig. 9.

The data points shown in Fig. 9 represent ordered PFCD arrays (O) generated using simultaneous dilatational strain and shear flow, at two different sample thicknesses, $d = 250\ \mu$m and $d = 400\ \mu$m. These radial distribution functions are compared with that of a disordered array (DO) generated using dilatational strain without subsequent shearing at a sample thickness of $d = 250\ \mu$m. In all three distribution functions, we observe a distinct series of peaks. The location of the first peak indicates the characteristic distance between the defects in the array, which is equivalent to the size of the defects since the PFCDs within the array fill the entire space. The peak height for the disordered array is lower and the peak width is broader than that of the ordered arrays, consistent with the reduced degree of ordering in the sample. A comparison of the locations of the first peak for the ordered defects indicates that as the sample thickness increases, the defect size also increases. The ordered arrays exhibit multiple peaks, while the disordered arrays exhibit a single broad peak with no obvious higher-order peaks. The higher-order peaks indicate long-range order that persists within the spatial limits of the image. Thus, the advantage of analyzing the defect size using the radial distribution function is that it provides an objective measure of the defect size and the breadth of the size distribution for both ordered and disordered defects, whereas previous manual measurements render it difficult to analyze these features in a statistically meaningful way.

In Fig. 10 we plot the defect sizes obtained from the locations of the first peaks of $g(r)$ as a function of the sample thickness. The sizes of the ordered defects are denoted by (Δ) and those of the disordered defects are denoted by ($\bullet$) symbols. In addition, the defect sizes measured by Oswald *et al.* [12] are plotted using ($\square$) symbols for comparison. The plot shows that the characteristic defect sizes of ordered and disordered textures are equivalent to within experimental uncertainty,

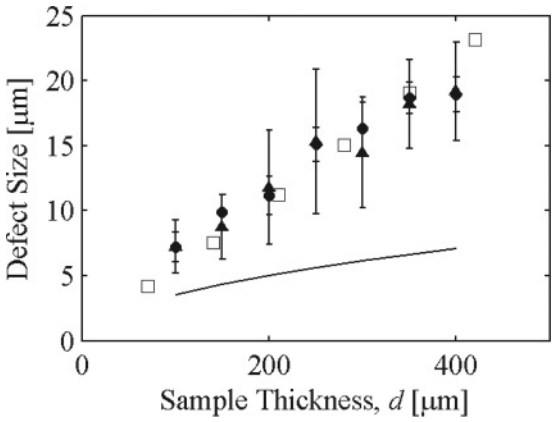

FIG. 10. Defect size as a function of the sample thickness. The triangles denote the sizes of disordered defects formed by dilatational strain alone, the circles denote the sizes of ordered defects formed by simultaneous dilatational strain and shear flow and the squares denote the experimental results of Oswald *et al.* [12]. The solid line corresponds to the predicted scaling from the undulation instability [18].

although as expected, ordered defects have a narrower size distribution than disordered defects. Our measured sizes for both ordered and disordered patterns are in good agreement with the defect sizes reported by Oswald *et al.* [12]. As these authors reported, the empirical defect sizes deviate both in magnitude and in scaling compared with the wavelength p of the undulation instability, [18] given by

$$p = \sqrt{2\pi\lambda d}. \tag{8}$$

The wavelength predicted for 8CB using the scaling of Eq. (8) is shown in Fig. 9 (solid line). Oswald *et al.* [12] fit an empirical function to their defect size data but did not offer a physical explanation for the differences observed. Our observation that the sizes of the disordered and ordered defects are the same indicates that ordering due to applied shear flow is not the reason for the change in scaling. Thus, we presume that the deviation of the defect sizes from that predicted by linear stability analysis is a result of the nonlinear growth of defects from the initial undulations. This result is consistent with the analytical predictions of Oswald and Ben-Abraham [16] that the critical wavelength of the undulations remains the same in the presence and absence of shear flow.

IV. CONCLUSIONS

In this study, we describe experimental observations of defect arrays formed using four different methods of deforming a smectic liquid crystal sample. The smectic liquid crystals are confined in a shear cell with homeotropic anchoring imposed on both plate surfaces. Defects are formed by applying dilatational strain alone, shear flow alone, dilatational strain and subsequent shear flow, and the simultaneous action of dilatational strain and shear flow. The latter method produces the most uniform and ordered arrays of parabolic focal conic defects. The defects are arranged in square arrays, consistent with previous experimental observations [12] as well as a linear stability analysis for smectic layer undulations in the presence of dilatational strain and shear flow [16].

When defects are formed by application of dilatational strain alone, PFCDs originate from within the sample, rather than at the surface. This is consistent with a mechanism [11] suggesting that defects are formed from sinusoidal layer undulations within the bulk of the sample. This is an important difference from the formation of defects based on a pure shear flow, where defects are formed as a result of surface irregularities.

By performing experiments over a range of sample thicknesses, we show that in the case of simultaneous application of dilatational strain and shear flow, the critical dilatation required for formation of visible defects is of the order of a few micrometers. While layer undulations are likely to occur in all the samples since undulations only require angstrom-level dilatations, the formation of visible defect textures requires dilatations that are about three orders of magnitude larger. Very thin samples require more dilatation to produce visible defects, suggesting that bulk elastic interactions dominate over surface anchoring conditions as sample thickness increases, and thus the relaxation of the layers into defects is easier for thicker samples.

We use the pair distribution function to quantify the order and size of the defect textures formed within the shear cell. The angular distribution function $g(\theta)$ confirms that the defects arrange in a square lattice in the presence of a shear flow. The angular distribution function also shows that there is systematically more ordering in the flow direction compared with the neutral direction, a result that is in contrast with previous theoretical predictions near the undulation threshold [16]. Closer analysis of images of the defect arrays reveals that this difference in ordering is a result of dislocations in the ordered array. These dislocations in the positional order of the topological defects are more prevalent in the neutral direction.

The radial distribution function is used to determine the characteristic defect sizes in disordered and ordered textures. Disordered textures, formed by dilatational strain only, exhibit a single broad peak indicating the absence of long-range order. This is contrary to linear stability analysis, which predicts the arrangement of undulations in square lattices [27]. The disordered textures show the same mean size as ordered textures and these sizes are consistent with previous measurements for ordered textures [12]. All of these measurements are different from the scaling of the wavelength of the undulations. The applied shear flow itself does not cause a change in defect sizes, since both ordered and disordered textures show the same scaling of sizes with sample thickness. We conclude that although the defects originate from layer undulations within the bulk of the sample, the development of the undulation instability far from the threshold leads to changes in size and ordering that are not predicted by linear stability theory. An analysis of the texture using the pair distribution function clearly establishes these changes in the size and ordering far from the stability threshold.

ACKNOWLEDGMENTS

We thank Steve Garoff, Alan McGaughey, and Lynn Walker for helpful discussions and suggestions. We are grateful for support from the National Science Foundation (NSF Grant No. CBET-0547432).

[1] P. G. de Gennes and J. Prost, *The Physics of Liquid Crystals* (Oxford University Press, New York, 1995).
[2] M. Delaye, R. Ribotta, and G. Durand, Phys. Lett. A **44**, 139 (1973).
[3] N. A. Clark and R. B. Meyer, Appl. Phys. Lett. **22**, 493 (1973).
[4] F. Brochard-Wyart and P. G. de Gennes, Science (NY) **300**, 441 (2003).
[5] L. Courbin, R. Pons, J. Rouch, and P. Panizza, Europhys. Lett. **61**, 275 (2003).
[6] A. G. Zilman and R. Granek, Eur. Phys. J. B **11**, 593 (1999).
[7] W. Helfrich, J. Chem. Phys. **55**, 839 (1971).
[8] Y. Cohen, M. Brinkmann, and E. L. Thomas, J. Chem. Phys. **114**, 984 (2001).
[9] I. I. Smalyukh, O. V. Zribi, J. C. Butler, O. D. Lavrentovich, and G. C. L. Wong, Phys. Rev. Lett. **96**, 177801 (2006).
[10] P. Oswald, J. C. Geminard, L. Lejcek, and L. Sallen, J. Phys. II **6**, 281 (1996).
[11] C. S. Rosenblatt, R. Pindak, N. A. Clark, and R. B. Meyer, J. Phys. **38**, 1105 (1977).
[12] P. P. Oswald, J. Behar, and M. Kleman, Philos. Mag. A **46**, 899 (1982).
[13] R. G. Horn and M. Kleman, Ann. Phys. **3**, 229 (1978).
[14] Y. H. Kim, J.-O. Lee, H. S. Jeong, J. H. Kim, E. K. Yoon, D. K. Yoon, J.-B. Yoon, and H.-T. Jung, Adv. Mater. **22**, 2416 (2010).
[15] Y. H. Kim, D. K. Yoon, H. S. Jeong, O. D. Lavrentovich, and H. T. Jung, Adv. Funct. Mater.
[16] P. Oswald and S. I. Ben-Abraham, J. Phys. **43**, 1193 (1982).
[17] J. B. Fournie and G. Durand, J. Phys. II **1**, 845 (1991).
[18] R. Ribotta and G. Durand, J. Phys. **38**, 179 (1977).
[19] N. A. Clark and A. J. Hurd, J. Phys. **43**, 1159 (1982).
[20] O. Diat, D. Roux, and F. Nallet, J. Phys. II **3**, 1427 (1993).
[21] A. S. Wunenburger, A. Colin, T. Colin, and D. Roux, Eur. Phys. J. E **2**, 277 (2000).
[22] S. A. Asher and P. S. Pershan, J. Phys. **40**, 161 (1979).
[23] C. Wolf and A. M. Menzel, J. Phys. Chem. B **112**, 5007 (2008).
[24] P. Oswald and P. Pieranski, *Smectic and Columnar Liquid Crystals: Concepts and Physical Properties Illustrated by Experiments* (CRC, Boca Raton, FL, 2006).
[25] G. Napoli and A. Nobili, Phys. Rev. E **80**, 031710 (2009).
[26] S. J. Singer, Phys. Rev. E **48**, 2796 (1993).
[27] J. M. Delrieu, J. Chem. Phys. **60**, 1081 (1974).
[28] S. I. Ben-Abraham, Mol. Cryst. Liq. Cryst. **123**, 77 (1985).
[29] P. Oswald, J. Phys. Lett. **44**, 303 (1983).
[30] R. G. Horn, Rev. Sci. Instrum. **50**, 659 (1979).
[31] R. G. Larson and P. T. Mather, in *Theoretical Challenges in the Dynamics of Complex Fluids*, edited by T. C. McLeish (Springer, Berlin, 1997).
[32] M. Yada, J. Fukuda, J. Yamamoto, and H. Yokoyama, Rheol. Acta **42**, 578 (2003).
[33] R. G. Larson and D. W. Mead, Liq. Cryst. **12**, 751 (1992).
[34] G. Platz and C. Thunig, Langmuir **12**, 1906 (1996).
[35] W. J. Benton, E. W. Toor, C. A. Miller, and T. Fort, J. Phys. **40**, 107 (1979).
[36] W. Benton and C. Miller, Prog. Colloid Polym. Sci. **68**, 71 (1983).
[37] A. M. Donald, C. Viney, and A. P. Ritter, Liq. Cryst. **1**, 287 (1986).
[38] M. Roman and D. G. Gray, Langmuir **21**, 5555 (2005).
[39] I. W. Stewart, Liq. Cryst. **15**, 859 (1993).
[40] J. Ignes-Mullol, J. Baudry, L. Lejcek, and P. Oswald, Phys. Rev. E **59**, 568 (1999).
[41] G. Bossis and J. F. Brady, J. Chem. Phys. **80**, 5141 (1984).
[42] O. D. Lavrentovich, M. Kleman, and V. M. Pergamenshchik, J. Phys. II **4**, 377 (1994).
[43] T. Shioda, B. Wen, and C. Rosenblatt, Phys. Rev. E **67**, 041706 (2003).
[44] J. B. Fournier, I. Dozov, and G. Durand, Phys. Rev. A **41**, 2252 (1990).
[45] P. M. Chaikin and T. C. Lubensky, *Principles of Condensed Matter Physics* (Cambridge University Press, Cambridge, 2000).
[46] A. D. Dinsmore, E. R. Weeks, V. Prasad, A. C. Levitt, and D. A. Weitz, Appl. Opt. **40**, 4152 (2001).
[47] G. E. Dieter and D. Bacon, *Mechanical Metallurgy*, Vol. 45 (McGraw-Hill, London, 1986).
[48] A. P. Marencic, M. W. Wu, A. Richard, and P. M. Chaikin, Macromolecules **40**, 7299 (2007).